Solar RRL
www.solar-rrl.com

Multiple Effects Induced by Mo^{6+} Doping in $BiVO_4$ Photoanodes

*Annalisa Polo, Maria Vittoria Dozzi, Ivan Grigioni, Charles Lhermitte, Nukorn Plainpan, Luca Moretti, Giulio Cerullo, Kevin Sivula, and Elena Selli**

Mo^{6+} doping increases the photoelectrochemical performance of $BiVO_4$ photoanodes in water oxidation. Herein, the underlying mechanisms is elucidated through a systematic structural, morphological, and photoelectrochemical investigation on photoelectrodes of pure and Mo^{6+} doped $BiVO_4$ prepared by a novel multistep spin-coating deposition approach, leading to multilayer flat films with high optical transparency. Transient absorption spectroscopy in the nano- to microsecond time scale reveals a longer lifetime of photogenerated holes in the doped films. Besides confirming that Mo^{6+} ions improve the electron transport in the material bulk, impedance spectroscopy also reveals the crucial role of the dopant on the surface properties of $BiVO_4$ photoanodes. The presence of intra-bandgap states, acting as traps of photogenerated charge carriers in pure $BiVO_4$, is detected through the build-up of the interfacial surface state capacitance. The limited activity of pure $BiVO_4$ in water oxidation is largely improved upon 3 at% Mo^{6+} incorporation, ensuring a more efficient charge carrier transport with respect to pure $BiVO_4$, together with the beneficial passivation of its trap surface states.

1. Introduction

Solar energy conversion enables to capture the freely available energy from sunlight and turn it into highly valuable and storable chemical fuels such as clean hydrogen from water.[1] Although artificial photosynthesis is the most promising approach to renewable energy for a sustainable society,[2] the development of simultaneously competitive, cost-effective, and efficient systems for storing solar energy in the chemical form on a global scale is still a great challenge.[3,4] The photoelectrochemical (PEC) tandem cell technology allows achieving solar-to-hydrogen conversions above 20% from water splitting by maximizing photon absorption in a two photoelectrode configuration able to harvest complementary portions of the solar spectrum,[5] with the photoanode layered on top of a smaller band gap photocathode efficiently exploiting the incoming photons and transmitting to the photocathode the photons less energetic than the photoanode material band gap.[6]

Among the semiconducting metal oxides to be employed as photoanodes in this architecture,[7] $BiVO_4$ (BV) emerged for its stability[8] and desirable visible light conversion efficiency due to its relatively narrow band gap energy (E_g) of 2.4 eV.[9] However, intrinsic limitations, such as poor charge transport,[10] slow water oxidation kinetics,[11,12] and a high rate of surface recombination,[12,13] hamper the achievement of the maximum theoretical photocurrent of 7.6 mA cm^{-2}. Nanostructuring may be an effective strategy to tackle the charge carrier transport limitations of $BiVO_4$ photoanodes,[14] but it compromises the high electrode transparency required for an efficient dual absorbers cell configuration.[6,15]

Doping $BiVO_4$ with metal ions higher valent with respect to both Bi^{3+} and V^{5+}, such as Mo^{6+} and W^{6+}, is the most successful strategy to increase the water oxidation activity of pure $BiVO_4$.[16,17] The observed PEC performance enhancement is usually associated with the alleviation of the intrinsic poor electron transport properties of the material, since the hexavalent ions can act as shallow donors supplying additional free electrons, thus increasing the majority carrier concentration and, consequently, the n-type conductivity in the bulk.[10,18,19] Doping with Mo was found to provide superior conductivity,[20] and therefore higher photoactivity,[16,17,21,22] than doping with W.

Other effects, such as crystal deformation, grain size growth, or the passivation of trap sites, were also invoked to account for the significant improvement in PEC performance observed upon Mo doping of $BiVO_4$,[20,23–28] which was usually found to depend on the dopant content and possibly result from the balance of different effects. In fact, beyond the processes affecting the material bulk, the chemistry at the semiconductor–liquid

A. Polo, M. V. Dozzi, I. Grigioni, E. Selli
Dipartimento di Chimica
Università degli Studi di Milano
20133 Milano, Italy
E-mail: elena.selli@unimi.it

C. Lhermitte, N. Plainpan, K. Sivula
Laboratory for Molecular Engineering of Optoelectronic Nanomaterials
École Polytechnique Fédérale de Lausanne (EPFL)
1015 Lausanne, Switzerland

L. Moretti, G. Cerullo
Department of Physics
Milan Polytechnic
20133 Milano, Italy

The ORCID identification number(s) for the author(s) of this article can be found under https://doi.org/10.1002/solr.202200349.

DOI: 10.1002/solr.202200349

junction (SCLJ) has a huge impact on the efficiency of PEC devices, especially when the performance is limited by a sluggish water oxidation kinetics, as in the case of $BiVO_4$. Surface states may consist of either intrinsic traps or photogenerated intermediate species of the water oxidation reaction, likely surface hydroxyl groups and high-valent metal-oxo complexes.[29] The unambiguous identification of the nature of surface states in metal oxide-based materials, of their location and role is still challenging, depending on the kind of metal oxide, its synthesis and/or annealing conditions and, eventually, on the nature of the dopant.

This work aims at identifying the mechanisms responsible for the PEC performance enhancement in water oxidation induced by Mo^{6+} doping of $BiVO_4$ photoanodes, through an in-depth investigation of the role of Mo^{6+} doping in modifying both the bulk properties of the material and the chemistry of surface states.[30] Photoelectrodes of pure and Mo^{6+}-doped $BiVO_4$ were prepared by means of a novel multistep spin-coating deposition approach, leading to multilayer flat films with high optical transparency, which is an important requirement for their implementation in the dual absorber PEC tandem devices. A systematic investigation was performed, employing a series of complementary structural and PEC investigation strategies, including transient absorption measurements providing information on the dynamics of photogenerated charge carriers in the semiconductor, to correlate the effects of photoactive film thickness and doping to the PEC performance in water oxidation. Three series of photoanodes with increasing thickness were prepared by depositing on conductive glass an increasing number of photoactive material thin layers, consisting of either pure $BiVO_4$ or Mo-doped $BiVO_4$. These were labeled nL_BV and nL_BV_X%, respectively, with n referring to the number of coating layers (L) and X standing for the nominal dopant molar ratio (X = 0.5 or 3, corresponding to 0.5 or 3.0 at% Mo).

2. Results and Discussion

2.1. Photoelectrodes Characterization

2.1.1. X-Ray Diffraction and Raman Characterization

The crystal structure and phase composition of the BV-based materials were ascertained by X-Ray diffraction (XRD) and Raman spectroscopy analyses of the thickest 8L electrodes, reported in **Figure 1**. All XRD traces shown in Figure 1a correspond to the standard pattern of monoclinic $BiVO_4$ (JCPDS 14-0688),[20,31,32] with the main characteristic (110), (121), and (040) diffraction peaks located at *ca.* 18.9°, 28.9°, and 30.5°, respectively. No patterns belonging to secondary phase impurities can be detected, except for the reflections relative to the fluorine-doped tin oxide (FTO) glass substrate (marked with asterisks in Figure 1a), which excludes the presence of traces of less active tetrahedron and rhombohedron phases.[33,34]

Thus, Mo^{6+} incorporation does not induce any phase change in monoclinic BV up to 3.0 at% Mo doping, in line with previous reports.[20,27,34–37] Moreover, no peaks relative to crystalline MoO_3 are detectable in the XRD patterns, suggesting the formation of a solid solution of Mo^{6+}-doped BV.[27,36,38] All XRD patterns exhibit sharp, relatively high-intensity peaks, indicating the high crystallinity of the films (Figure 1a). A slight (*ca.* 0.1°) shift of the (040) peak is observed for highly doped 8L_BV_3%, which can be ascribed to the compressive lattice strain induced by substitution of Mo^{6+} ions for relatively smaller V^{5+} ions[32,36] (having 0.41 and 0.35 Å ionic radius,[20] respectively), causing the partial distortion of the VO_4^{3-} tetrahedron space lattice. This should enhance the electron mobility of $BiVO_4$[23] and suggests the successful incorporation of Mo into the $BiVO_4$ lattice.[39] Furthermore, the progressive intensity increase of the XRD reflection at $2\theta = 18.9°$ with increasing Mo dopant content (Figure 1a) is in line with a progressive preferential growth along the (110) and (010) directions.[24]

The Raman spectra of both pure and doped BV (Figure 1b) exhibit the typical modes of the monoclinic phase of $BiVO_4$,[35,36] consistently with XRD analysis results. The dominant Raman band at *ca.* 827 cm^{-1} is assigned to the symmetric δ_s(V–O) stretching mode of the VO_4^{3-} units and the weak shoulder at *ca.* 710 cm^{-1} to the corresponding δ_{as} (V–O) asymmetric mode. The weak bands at around 325 and 360 cm^{-1} are identified as the asymmetric $\delta_{as}(VO_4^{3-})$ and symmetric $\delta_s(VO_4^{3-})$ deformation modes of VO_4^{3-}, respectively, while the band at around 210 cm^{-1} is ascribed to external (rotational or translational) modes. The progressive red shift of the δ_s(V–O) stretching mode with increasing Mo^{6+} dopant amount, passing from 827 cm^{-1} for pure 8L_BV to 820 cm^{-1} for 8L_BV_3%, also results from the Mo^{6+} for V^{5+} replacement in the $BiVO_4$

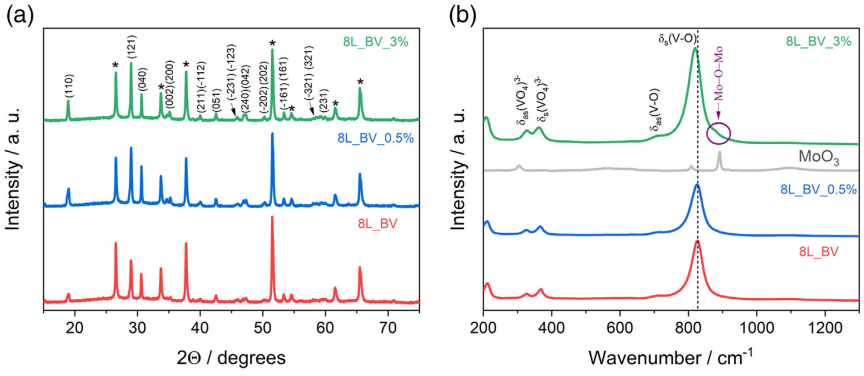

Figure 1. a) X-Ray diffraction (XRD) patterns and b) Raman spectra of 8L_BV, 8L_BV_0.5%, and 8L_BV_3%. The reflections relative to the fluorine-doped tin oxide (FTO) substrate are marked with an asterisk. The Raman spectrum of MoO_3 (gray trace) is also reported for comparison.

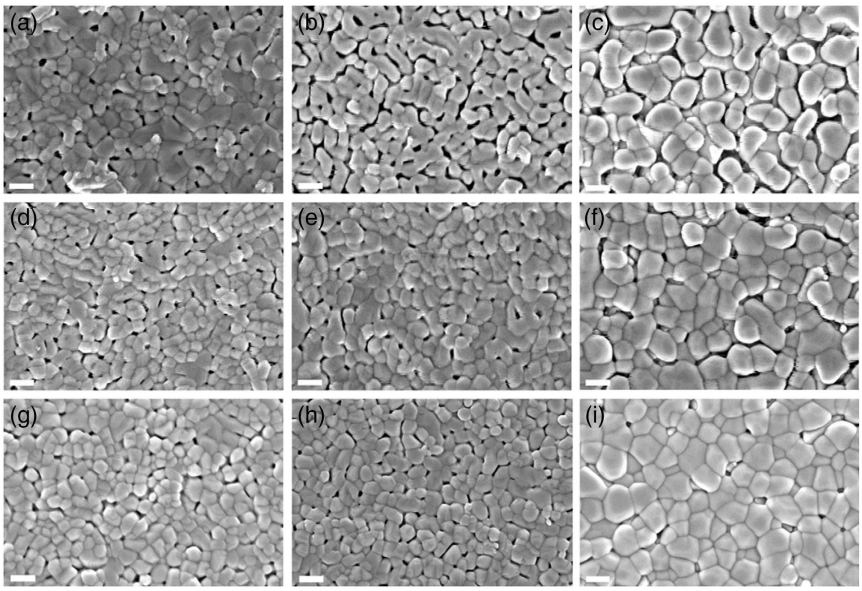

Figure 2. Top-down scanning electron microscope (SEM) images with high magnification (50.00 KX) of: a) 4L_BV, b) 4L_BV_0.5%, c) 4L_BV_3%, d) 6L_BV, e) 6L_BV_0.5%, f) 6L_BV_3%, g) 8L_BV, h) 8L_BV_0.5%, and i) 8L_BV_3%. The scale bar is 200 nm.

lattice,[17,19,21,24,34–36,38] causing elongation of the V–O bond in the VO_4 unit due to the larger ionic radius of Mo^{6+} compared to V^{5+}.[20] Also, the small shoulder appearing at 890 cm^{-1} in the Raman spectrum of 8L_BV_3%, coinciding with the Mo–O–Mo stretching mode[33,35,38] in the Raman spectrum of pure MoO_3 also reported in Figure 1b, is an indication of Mo^{6+} for V^{5+} substitution.

2.1.2. Morphological Characterization

The top-down low magnification scanning electron microscope (SEM) images of the 8L_BV, 8L_BV_0.5%, and 8L_BV_3% electrodes (Figure S1, Supporting Information) account for a flat surface with uniform texture, composed of densely packed, ~100–200 nm sized grains, indicating a homogeneous and compact coverage of the rough FTO surface.

The high magnification images relative to the 4, 6, and 8L films with different Mo dopant contents (0, 0.5, and 3 at%) are compared in **Figure 2**. A worm-like structure typical of BV films[30] is detected for the pure and 0.5 at% Mo^{6+}-doped films up to 6L, which progressively turns into a spherical shape morphology with increasing dopant amount and/or number of coating layers.

As evidenced by the estimated nanoparticles size in the films reported in **Table 1**, for a fixed number of coating layers a progressive increase in grain size is observed with increasing dopant amount, possibly consequent to a Mo^{6+}-induced particles agglomeration process,[24,27,35] the most significant increment in nanoparticles average size compared to pure BV being attained with 3 at% doped BV. For a fixed nominal dopant amount no mean particle size increase occurs with the increasing number of coatings, except for the 8L_BV_3% photoanode, exhibiting a *ca.* 20% larger average grain size compared to 4L_BV_3% and 6L_BV_3%. These trends suggest that the Mo^{6+} dopant acts as a nucleation site for interparticle aggregation,[40] especially when present in relatively high amount (i.e., 3 at%), leading to a denser film structure with a reduced number of free pin-holes between the sintered particles compared to pure BV. Moreover, a relatively high (3 at%) Mo^{6+} dopant content can also promote nanoparticles sintering between adjacent layers, as reflected by the abrupt increase in grain size observed when passing from 6 to 8 layers (Table 1).

Table 1. Films grain size, in nm, determined from the images shown in Figure 2.

Electrode	4L	6L	8L
BV	107 ± 14	105 ± 16	104 ± 15
BV_0.5%	114 ± 16	122 ± 22	114 ± 13
BV_3%	160 ± 28	160 ± 23	194 ± 30

Notably, the feature sizes reported in Table 1 are comparable with the typical 70–100 nm charge diffusion length reported for $BiVO_4$-based electrodes,[19,41,42] with only the 3 at% Mo^{6+} doped series (4L_BV_3%, 6L_BV_3%, and 8L_BV_3% electrodes) having grain sizes far above this threshold value.

The trend in grain size is reflected by the change in the real surface area of the electrodes, in terms of electrochemical active surface area (ECSA) determined, as detailed in the Supporting Information, through cyclic voltammetry measurements such as those shown in Figure S2, Supporting Information. Relative ECSA values, i.e., normalized with respect to that of the thinnest 4L_BV electrode, are collected in Table S1, Supporting Information. An ECSA decrease is observed with increasing Mo^{6+} dopant content for a fixed number of layers, the highest variation being attained with the 8L films, while only a slight decrease in ECSA occurs when increasing the number of layers, this trend becoming progressively more evident with increasing Mo^{6+} dopant content.

The average film thickness of the thickest 8-layered photoanodes, evaluated by means of SEM cross-section images (**Figure 3**), is *ca.* 150 ± 15 nm, independent of the dopant amount, i.e., slightly lower than the average particles sizes detected for the 8L_BV_3% film, suggesting a preferential film growth parallel to the FTO substrate.

The atomic force microscope (AFM) images shown in Figure S3, Supporting Information, confirm the spherical shape of the nanoparticles composing 8L films, as well as the grain coalescence with increasing dopant amount, while the 3D surface topography images, also reported in Figure S3, Supporting Information, reveal the presence of distinctive reliefs on the film surface, becoming progressively more extended and sharper as the particles dimension increases with increasing dopant amount. In parallel, the surface roughness, estimated through the root mean square (RMS) factor reported in Figure S3, Supporting Information, also increases with increasing dopant amount.

2.1.3. Optical Characterization

The absorption coefficients (α) at 420 nm of pure BV and of 0.5 at%- and 3 at%-doped BV were estimated on the basis of the Lambert–Beer law[43,44] from the absorbance at 420 nm of the thickest 8L electrode of each series (see Figure S4, Supporting Information) and their thickness evaluated from the cross-section images shown in Figure 3. The so determined α_{420nm} values are 0.015, 0.020, and 0.023 nm^{-1} for pure BV, 0.5 at%, and 3 at% Mo^{6+} doped films, respectively. The thickness of all investigated photoanodes, estimated from the α_{420nm} values and the absorbance of the photoactive films at 420 nm, are collected in Table S2, Supporting Information.

From the estimated absorption coefficients at 420 nm, the light penetration depth values were calculated, corresponding to film thicknesses ensuring 96%, 83%, and 63% absorption of the incident 420 nm radiation, as $\delta_{96\%} = 3\,\alpha^{-1}$, $\delta_{83\%} = 2\,\alpha^{-1}$ and $\delta_{63\%} = \alpha^{-1}$, respectively.[44] The obtained values for 8L films are reported in Table S3, Supporting Information. The δ value accounting for 96% absorption of incident 420 nm photons, *ca.* 200 nm for the 8L_BV electrode, in perfect agreement with literature values,[42,44,45] decreases to *ca.* 150 and 130 nm in the case of the 8L_BV_0.5%, and 8L_BV_3% doped systems, respectively.

The above reported α_{420nm} values indicate that Mo doping decreases the fraction of light transmitted through our BV films. Indeed, the absorption spectra of the 8L electrodes shown in Figure S4, Supporting Information evidence that the absorbance of Mo-containing films at wavelengths shorter than the $BiVO_4$ absorption edge (*ca.* 520 nm for a 2.4 eV bandgap) is higher than that of the undoped BV film, though without any change in spectral shape. Thus, the apparent absorbance increase with increasing Mo^{6+} content should be correlated to the grain size enlargement in the films, causing scattering effects, reflected by a slightly higher opacity of 3 at% Mo^{6+}-doped films, rather than to band gap energy narrowing of the material.

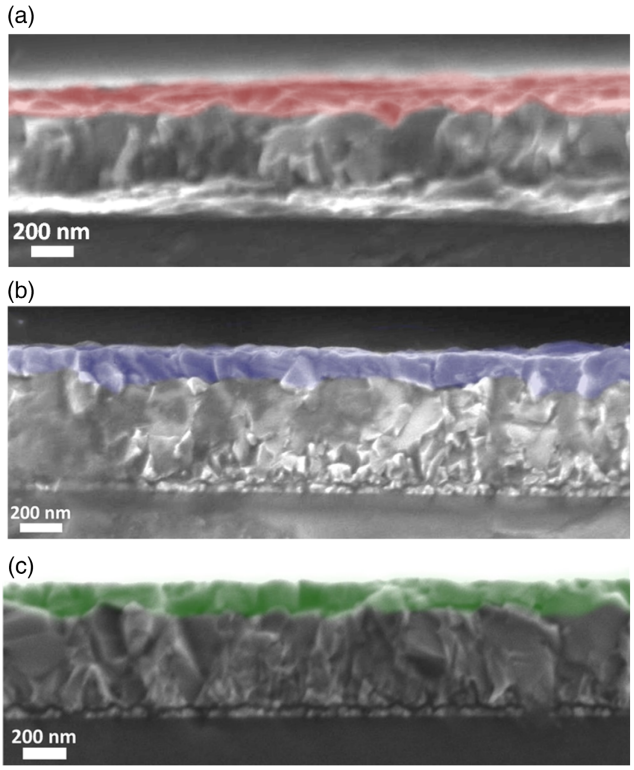

Figure 3. Cross section images of: a) 8L_BV, b) 8L_BV_0.5%, and c) 8L_BV_3%.

2.1.4. X-Ray Photoelectron Spectroscopy Characterization

The elemental surface composition of 8L films was finally investigated by X-Ray photoelectron spectroscopy (XPS). Survey spectra confirmed the presence of Bi, V, O, and Mo, and no other elements, apart from adventitious carbon. The XPS spectra in the binding energy (BE) regions of Bi 4f, V 2p, O 1s, and Mo 3d are shown in **Figure 4**. The characteristic spin–orbit doublet separation of the Bi 4f ($Bi4f_{5/2}$ and $Bi4f_{7/2}$) and V 2p ($V2p_{1/2}$ and $V2p_{3/2}$) signals typical of monoclinic scheelite $BiVO_4$[23,25,46,47] can be observed in Figure 4a,b, with the Bi $4f_{7/2}$ and Bi $4f_{5/2}$ core level peaks at BE 158.9 and 164.3 eV, respectively (Figure 4a), confirming the presence of Bi^{3+} cations, and the V $2p_{3/2}$ and V $2p_{1/2}$ core level peaks at BE 516.7 and 524.3 eV, respectively (Figure 4b), allowing unambiguous assignment to V^{5+}.

The O 1s signal (Figure 4c) at *ca.* 529.7 eV is assigned to lattice oxygen (V–O) and the shoulder at around 532 eV to oxygen vacancies and hydroxyl groups (−OH) on the $BiVO_4$ film surface,[39,48,49] which can act as surface hole trapping sites or intermediates of the oxygen evolution reaction.[48,49] This shoulder is most evident in the XPS spectrum of 8L_BV and almost disappears in the XPS signal of 8L_BV_3% (Figure 4c), indicating a lower concentration of oxygen vacancies and surface −OH groups upon 3 at% Mo^{6+} incorporation.

Definite evidence of successful Mo^{6+} doping is provided by the presence of the two characteristic Mo $3d_{5/2}$ and $3d_{3/2}$ peaks, located at 232.1 and 235.1 eV, respectively, only in the XPS spectra of the two doped photoanodes (Figure 4d), with intensity increasing with increasing nominal doping degree.[23,34,40,46,47,50]

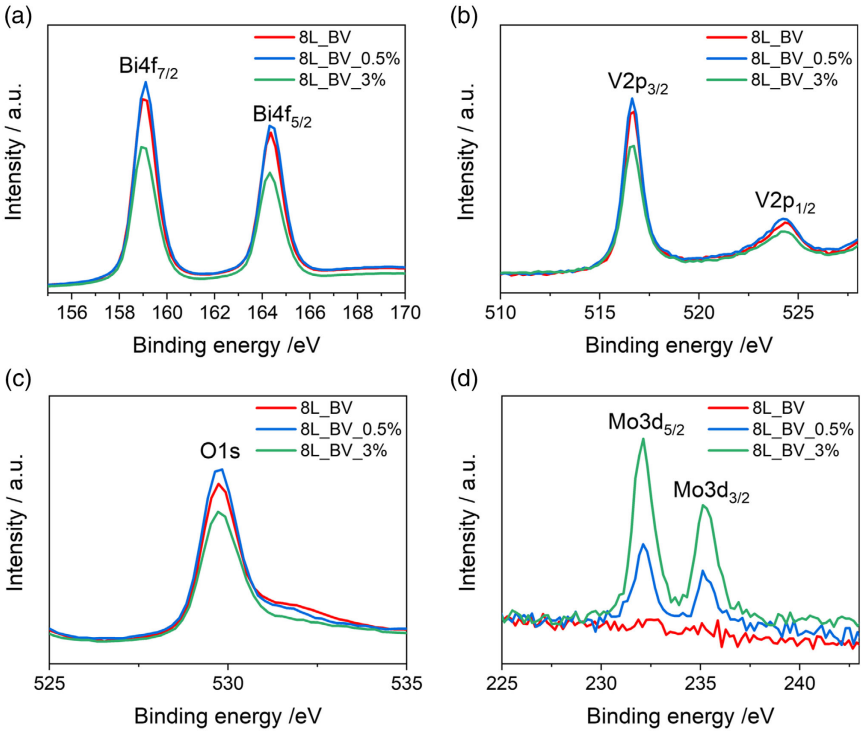

Figure 4. X-Ray photoelectron spectroscopy (XPS) spectra of the 8L films in the binding energy regions of the: a) Bi 4f, b) Mo 3d, c) V 2p, and d) O 1s signals.

The composition of the 8L films was also investigated at different depths from the surface, by acquiring the XPS spectra after etching with Ar^+ ions sputtering. The so recorded spectra of the doped electrodes in the Mo 3d binding energy region are collected in **Figure 5**, while those in the Bi 4f, V 2p, C 1s, and O 1s BE regions are reported in Figure S5–S7, Supporting Information.

Notably, for both 8L_BV_0.5% (Figure 5a) and 8L_BV_3% (Figure 5b), the intensity of the Mo 3d XPS signal decreases with increasing etching depth, the Mo content in the bulk being below the detection limit of XPS analysis. Gradient doping is thus evidenced, with Mo^{6+} ions being confined at the top of the film surface, especially in the case of 0.5 at% Mo doping.

The actual Mo:(V + Bi) surface atomic ratios obtained for the 8L_BV_0.5% and 8L_BV_3% electrodes (**Table 2**) are slightly higher than the nominal ones, as observed elsewhere,[21,37,46,47] which is the first indication of Mo-rich surface photoanodes, confirmed by the dramatic Mo:(V + Bi) atomic ratio decrease obtained upon etching. This phenomenon was attributed to Mo surface segregation at high temperatures driven by sublimation of Mo oxides.[21,46,47,51]

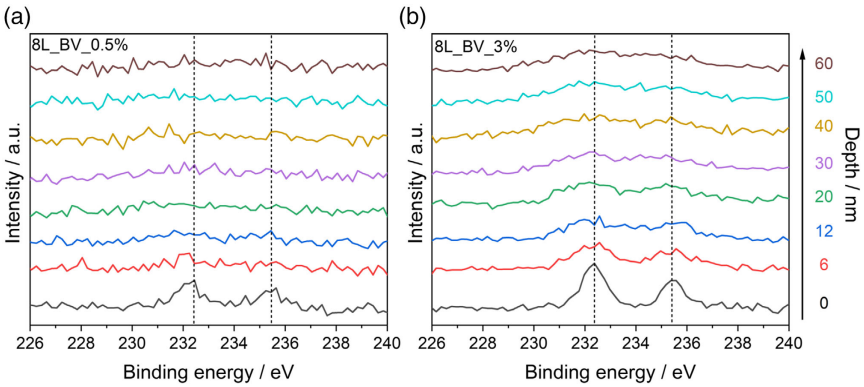

Figure 5. XPS spectra in the Mo 3d binding energy region of: a) 8L_BV_0.5% and b) 8L_BV_3%, before (black line) and after Ar^+ ions sputtering at progressively increasing etching depth, in the 6 (red line) to 60 nm (brown line) range.

Table 2. Relative atomic ratios from XPS analyses of the 8L films before and after etching.

	Mo:(Bi+V)	
Material	Surface	60 nm depth
BV	0	0
BV_Mo_0.5%	1.4%	0.3%
BV_Mo_3%	3.8%	2.1%

2.2. Transient Absorption Spectroscopy (TAS)

The charge carrier dynamics of the $BiVO_4$-based multilayer photoanodes was investigated through TAS in the nanosecond to microsecond time scale,[52] by recording the differential absorption (ΔA) signal evolution for pure BV and for the doped materials. In particular, in the present work, we monitored the photoinduced absorption feature of $BiVO_4$ at 470 nm, attributed to photoproduced holes trapped in $BiVO_4$ intra-bandgap (IBG) states. Their trapping occurs within 5 ps after excitation, which is beyond the lower limit of the here employed time window.[22,52–56]

The normalized ΔA decay traces probed at 470 nm for each of the multilayer electrode series are compared in Figure S8, Supporting Information as a function of the film thickness on the 100 µs time scale. In all cases the ΔA signal completely decays on this time scale, allowing a direct comparison of the dynamics of photoproduced holes in different electrodes.

Figure 6 shows the magnification of the ΔA signals at 470 nm on a 200 ns time scale, which was successfully fitted using a biexponential decay model, according to Equation (1)

$$\Delta A = A_1 e^{-t/\tau_1} + A_2 e^{-t/\tau_2} + \Delta A_0 \quad (1)$$

where τ_1 and τ_2 are the time constants of the faster and slower decay processes, respectively, A_1 and A_2 are the weighted amplitudes of the contribution of each of the two processes to the overall decay, and ΔA_0 is the signal offset. The ΔA signal almost totally decays on the 200 ns time scale, although zero ΔA_0 values were reached only in the case of pure BV. The corresponding fitting parameters are reported in **Table 3**.

Table 3. Fitting parameters, according to Equation (1), of the ΔA transient decay tracked at 470 nm upon excitation of all BV-based multilayer electrodes.

	A_1 [%]	τ_1 [ns]	A_2 [%]	τ_2 [ns]
BV_4L	75.7 ± 0.7	4.82 ± 0.10	24.3 ± 0.6	52 ± 2
BV_6L	78.6 ± 0.6	6.26 ± 0.09	21.4 ± 0.6	58 ± 2
BV_8L	77.8 ± 0.6	9.11 ± 0.13	22.2 ± 0.6	82 ± 3
BV_4L_0.5%	80.5 ± 0.5	8.72 ± 0.12	19.5 ± 0.4	137 ± 7
BV_6L_0.5%	81.1 ± 0.3	13.0 ± 0.11	18.9 ± 0.3	203 ± 8
BV_8L_0.5%	80.7 ± 0.4	20.36 ± 0.18	19.3 ± 0.3	290 ± 15
BV_4L_3%	81.4 ± 0.6	6.45 ± 0.11	18.6 ± 0.5	95 ± 5
BV_6L_3%	84.3 ± 0.5	10.45 ± 0.12	15.7 ± 0.4	140 ± 8
BV_8L_3%	85.7 ± 0.3	15.24 ± 0.11	14.3 ± 0.3	191 ± 9

Direct comparison of the obtained fitting parameters within each film series with constant doping degree and different thickness is allowed by the almost unchanged grain size with an increasing thickness (see Table 1). In contrast, due to the non-negligible increase in particle size occurring with increasing Mo^{6+} dopant content at constant film thickness, morphological features may affect the charge carrier dynamics in electrodes with different doping degrees.

Upon photoexcitation with the here employed 240 µJ cm^{-2} fluence, most trapped holes recombine within 5–20 ns, regardless of the film thickness and doping degree, as indicated by the much larger A_1 values (in the 76–86% range) compared to the A_2 values (14–24%) reported in Table 3. While the relative weights of the two decay processes are almost unaffected by the film thickness, a progressive increase of both τ_1 and τ_2 is observed with an increasing number of photoactive layers (Table 3). Thus, IBG-trapped holes recombination with both thermalized (τ_1) or longer lived trapped electrons (τ_2) occurs faster in thinner films, where a lower fraction of holes are photogenerated in the material bulk. An analogous behavior was recently observed for zinc ferrite photoanodes with a similar planar morphology.[57]

As for the effect of Mo^{6+} doping on the charge carrier dynamics, in doped materials both τ_1 and τ_2 are longer than

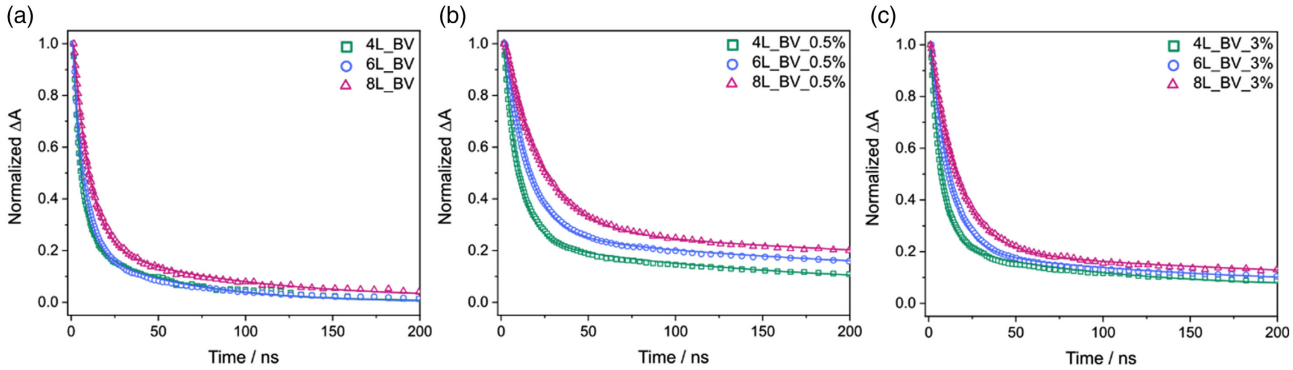

Figure 6. Normalized ΔA transient decay tracked at 470 nm for: a) pure BV, b) 0.5%-doped, and c) 3%-doped BV electrodes with 4L (green squares), 6L (blue circles), and 8L (red triangles) and the corresponding biexponential fittings traces (Equation (1)).

in pure BV for a fixed number of coating layers, indicating an increased charge separation efficiency. The τ_1 and τ_2 values obtained for 0.5%-doped BV are longer than those obtained for 3%-doped BV. However, also the relative weights of the two time constants should be taken into account, in the light of the different average grain sizes and morphology attained in the presence of different dopant amounts. In fact, as shown in Table 3, the average weight of the fast decay component, A_1, increases in the order 0, 0.5%, and 3% Mo doping, i.e., with increasing average particle size in the material (see Table 1), indicating that the fast decay component should be associated to hole recombination in the bulk material. Thus, increased charge separation (longest τ_1 and τ_2 values) results from an optimal balance between doping effects and film morphology, grain size, etc. being maximum in the thickest 0.5% Mo-doped BV_8L_0.5% electrode, having a much smaller grain size than the corresponding thickest 3 at% Mo-doped BV_8L_3% electrode (see Table 1).

2.3. Photoelectrochemical Performance of Multilayer Films

2.3.1. Linear Sweep Voltammetry

The PEC performance of all investigated multilayer films employed as photoanodes for water oxidation was checked in a 0.5 M Na_2SO_4 electrolyte solution by performing consecutive linear sweep voltammetry (LSV) scans under AM 1.5 G solar simulating light under both back- (through the FTO back-contact) and front-side (through the film/electrolyte interface) irradiation configurations. The photocurrent was stable for at least 10 scans and reproducible for several months. The last scans acquired with intermittent illumination for all investigated electrodes are collected in Figure S9, Supporting Information (up to 3 layers), and in **Figure 7** (4, 6, and 8L electrodes).

In pure BV electrodes, a progressive slight photocurrent increase is observed with an increasing number of coating layers up to 6L, under both back- and front-side irradiation, followed by an abrupt increase when passing from the 6L to the 8L electrode. This behavior can be related to the almost complete light absorption of the thickest (*ca.* 150 nm thick) 8L film (see Table S3, Supporting Information), though other factors may come into play. In fact, at low thickness the PEC performance may be limited by poor photon absorption, while with increasing photoactive film thickness, a significant increase in photocurrent occurs, once the film thickness exceeds an inactive layer depth, which is a signature of the so-called "dead-layer effect" observed for both thin $BiVO_4$ (thickness $\leq$ 125 nm)[58] and hematite films.[59,60] This phenomenon, arising from lattice mismatch at the film/FTO interface, results from the formation of amorphous, rich in trap states, material near the interface, which can be mitigated by SnO_2[61,62] or WO_3 underlayers.[58]

As to morphology effects, the more regular spherical shape of the nanoparticles composing the 8L film (Figure 2g), in comparison to 4 and 6L electrodes (Figure 2a,d), implies a lower number of grain boundaries responsible for charge recombination, which can explain the steep photocurrent density jump observed in Figure 7 when passing from the 6L_BV to the thickest 8L_BV electrode, which exhibits the highest photocurrent among the undoped BV electrodes under both illumination configurations.

Mo^{6+}-doped BV electrodes produce considerably higher photocurrent with respect to pure BV under both irradiation configurations, indicating that molybdenum doping helps overcoming the "dead-layer effect" impacting pure BV. Moreover, while a typical monotonic photocurrent increase with increasing

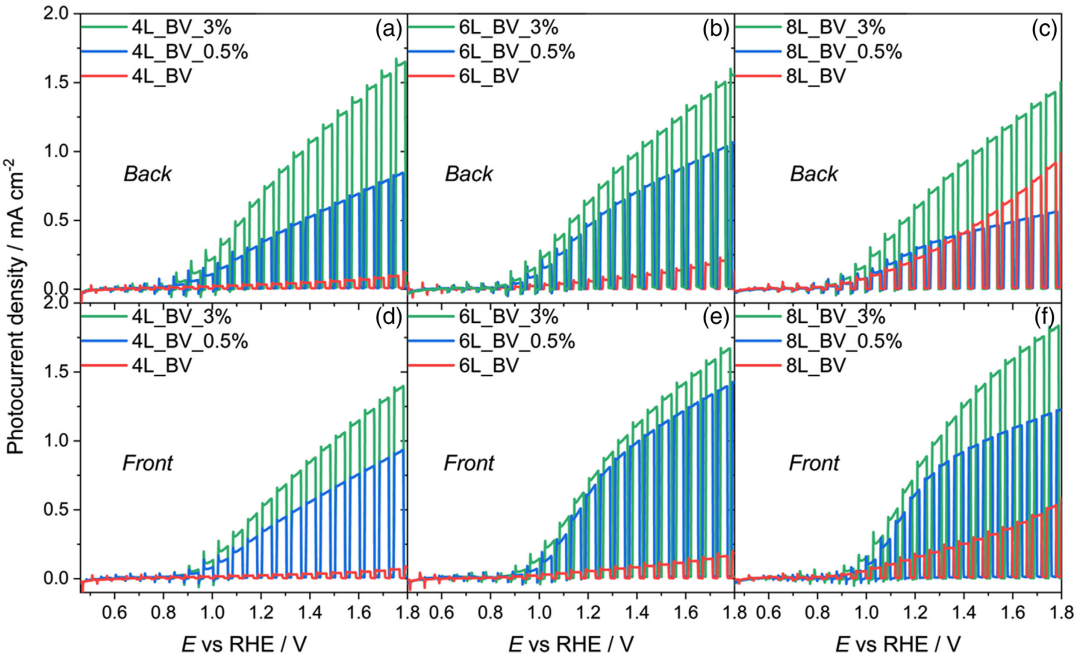

Figure 7. Linear sweep voltammetry (LSV) scans of the: a,d) 4L, b,e) 6L, and c,f) 8L electrodes under a–c) back- and d–f) front-side irradiation in a 0.5 M Na_2SO_4 electrolyte solution.

applied potential characterizes the *J*–*V* curves collected with pure BV, a better fill factor with a steeper photocurrent onset in the low applied potential region is obtained with doped electrodes, regardless of the dopant amount (Figure 7).

The dependence of photocurrent on the irradiation side of the electrodes is diagnostic of electron or hole transport limitations in the bulk of the material. **Figure 8** shows the photocurrent densities recorded under either front- or back-side irradiation at the reference potential of 1.23 V versus reversible hydrogen electrode (RHE) as a function of the number of coating layers in the three photoanodes series. Pure BV photoanodes produce relatively low photocurrent values, monotonically increasing with an increasing number of coating layers under both irradiation configurations, with comparable values under back- and front-side irradiation up to a 150 nm thickness, while the 8L_BV electrode generates a considerably higher photocurrent density when irradiated in back- rather than in front-side configuration.

Under back-side irradiation, a high density of charge carriers is photoproduced close to the FTO back-contact and electrons can be directly injected into the external circuit, which is an advantage in the case of materials suffering from poor electron transport, such as $BiVO_4$.[9,11,25,61] Therefore, the behavior observed with the thickest 8L_BV electrode reflects the bulk electron transport issues limiting the performance of pure BV when the thickness of the photoactive layer exceeds the *ca.* 70–100 nm typical $BiVO_4$ charge diffusion length.[42] For this reason, the photocurrent produced under back-side irradiation in pure BV photoanodes thicker than 100 nm (i.e., the 8L_BV electrode) exceeds that produced under front-side irradiation, reflecting the intrinsic limitations imposed by electron mobility within the photoactive layer.[11,61]

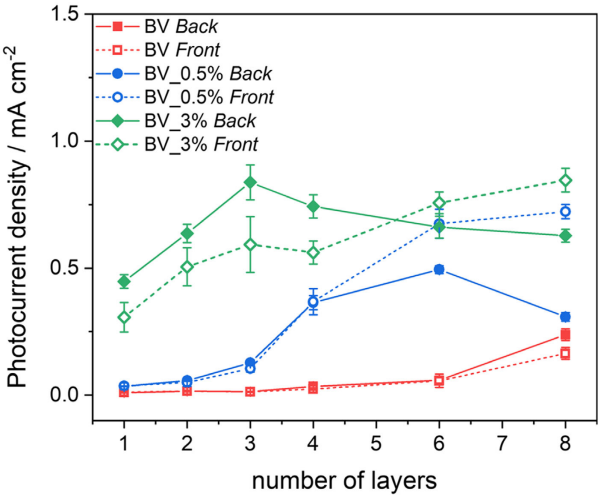

Figure 8. Photocurrent density at 1.23 V versus RHE, with relative error bars, versus. the number of coating layers for pure BV (red squares) and for the doped BV_0.5% (blue circles) and BV_3% (green diamonds) series, under back- (full symbols) and front-side (open symbols) irradiation, in a 0.5 M Na_2SO_4 solution. The error bars were calculated as the standard deviation of the values extracted from 5 distinct LSV scans. Continuous and dashed lines are just guides for the eye.

Conversely, for the two series of Mo^{6+} doped multilayer films the photocurrent density under front-side irradiation progressively increases with an increasing number of coating layers (Figure 8) and 6 and 8L films produce higher photocurrent under front- than under back-side irradiation. Indeed, under front-side irradiation a large density of charge carriers is photogenerated near the SCLJ and electrons have to travel a longer distance across the material bulk before reaching the FTO back-contact to the external circuit. Therefore, the better performance under front- rather than back-side configuration characterizing the thickest films of the two doped series (compare, for instance, Figure 7c with 7f) provides a clear indication of the largely improved electron transport produced by Mo^{6+} incorporation in $BiVO_4$, poor electron transport in the material bulk being no longer limiting for photocurrent production.[22,38,41]

The performance trend outlined for the Mo^{6+}-doped photoanodes in Figure 7 and S9, Supporting Information, thus results from morphological, optical, and electronic effects produced by doping. When the transport of the majority charge carriers (electrons in n-type semiconductors) in the bulk is no longer limiting due to the presence of the Mo dopant, the PEC performance of $BiVO_4$ is maximized by an optimal compromise between photon absorption depth and minority charge carriers (holes in n-type semiconductors) diffusion length.[24] In fact, Figure 8 evidences that under front-side irradiation BV_3% electrodes show a progressive photocurrent increase with increasing number of layers, attaining a maximum value with the thickest 8L_BV_3% electrode, which ensures almost complete light absorption. On the other side, these electrodes have a highly packed structure and they become more compact with increasing number of coating layers, which limits the exposition of the material to the electrolyte (see ECSA values in Table S1, Supporting Information). Thus, hole diffusion toward the film/electrolyte interface becomes progressively more hampered with increasing film thickness, with the consequent increase of electron–hole recombination probability. For this reason, the performance of the BV_3% electrodes under back-side irradiation is maximum for 70–90 nm thick films, i.e., for 3L_BV_3% (Figure 8), in which the distance that photogenerated holes need to travel to reach the film/electrolyte interface is comparable to their diffusion length in $BiVO_4$.[19,42] Thicker electrodes become relatively less performing under back-side irradiation. This highlights that under such conditions the PEC performance of Mo^{6+} doped $BiVO_4$ photoanodes is mainly limited by the hole diffusion length.

2.3.2. Incident Photon to Current Efficiency

The incident photon to current efficiency (IPCE) analyses recorded under front-side irradiation at 1.23 V versus RHE with the 8L_BV, 8L_BV_0.5%, and 8L_BV_3% photoanodes (Figure S10a) show pretty similar IPCE curve onsets at *ca.* 520–530 nm for all tested materials, confirming that Mo doping does not affect the bandgap energy of BV,[34,63] in line with the absorption spectra reported in Figure S4, Supporting Information. The IPCE values attained upon Mo^{6+} doping are

10-fold higher than those obtained with pure BV, with a 30% IPCE recorded at 420 nm for both 8L_BV_0.5% and 8L_BV_3% electrodes to be compared with 3% IPCE measured with pure 8L_BV. Furthermore, the IPCE curves (Figure S10a, Supporting Information) are almost superimposed on the internal quantum efficiency (IQE) plots (Figure S10b, Supporting Information), due to the almost quantitative absorption of incident photons by the 8L thick films.

Figure 9 shows the IPCE plots recorded with the 8L electrodes under back- and front-side irradiation, which confirm the results obtained in LSV measurements, i.e., that doped materials perform much better under front- rather than under back-side irradiation (Figure 9b,c), while the opposite is observed with pure 8L_BV (Figure 9a).

To check the compatibility of the two types of PEC analysis, the photocurrent density measured with the 8L electrodes at 1.23 V versus RHE was compared with that calculated by integrating the product of the corresponding IPCE curve (Figure 9) and the global AM 1.5 G solar spectral irradiation[11,64,65] over the 300–520 nm wavelengths range, under back- and front-side irradiation. The values, reported in Table S4, Supporting Information, show that both calculated and experimental photocurrent values progressively increase with increasing Mo^{6+} doping content, the calculated photocurrent values being slightly higher than the corresponding values measured under AM 1.5 G irradiation for the doped electrodes, while a better matching occurs for pure BV (Table S4, Supporting Information). The photoresponse recorded under relatively high AM 1.5 G light intensity is mainly affected by the slow oxygen evolution kinetics, because of the larger amount of electron-hole couples photogenerated under such conditions.[11] Differently, under the lower light intensity employed in IPCE measurements, the performance becomes limited by the $BiVO_4$ poor electron transport properties. This discrepancy between experimental and calculated values for the doped electrodes is larger under front- than under back-side configuration (see Table S4, Supporting Information), in line with the enhanced electron transport properties of $BiVO_4$ gained upon Mo doping, which becomes more evident under the low light intensity irradiation employed in IPCE analyses.

2.4. Electrochemical Impedance Spectroscopy

The remarkably enhanced photoactivity in water oxidation achieved upon Mo^{6+} doping cannot be fully explained only in terms of improved electron transport in the material bulk. Indeed, hexavalent Mo^{6+} ions modify not only the bulk but also the surface properties of $BiVO_4$. Aiming at evidencing the effects induced by Mo^{6+} doping on the material surface,[29,66–69] we performed an electrochemical impedance spectroscopy (EIS) analysis with the 8L_BV and 8L_BV_3% electrodes in contact with a Na_2SO_4 solution, either in the dark (EIS), or under the same conditions as LSV tests, i.e., under AM 1.5 G irradiation (photoelectrochemical impedance spectroscopy, PEIS).

The impedance spectra recorded with the two photoanodes at three representative applied potentials in the dark and under irradiation are shown in Figure S11a,b, Supporting Information, respectively, in the form of Nyquist plots. EIS spectra recorded in the dark display a single semicircle and their interpretation can be based on the Randles circuit model, by taking into account only the dielectric capacitance contribution, corresponding to the transfer of charges from the bulk of the semiconductor layer to the photoanode/electrolyte interface through the SCLJ. In contrast, each spectrum recorded under irradiation at a specific potential is in principle composed of two semicircles,[29,66,67] the semicircle at high frequency corresponding to the electrical response in the space charge region, which provides information on the charge transfer from the film bulk to the material/electrolyte interface, the low-frequency semicircle describing instead the interfacial charge transfer behavior at the SCLJ.[66] Therefore, a model considering both bulk and surface contributions is required to fit the impedance spectra under irradiation[29] and extract information on the electric properties described by the two semicircles.

The here employed circuit model is shown in the inset of **Figure 10**a. It was already employed for other metal oxide systems[29,66,67] including W–Ti-doped $BiVO_4$ photoanodes[70] and consists of: i) a series resistance R_S associated with charge transfer through the external circuit and the semiconductor bulk; ii) a bulk capacitance C_{bulk} (with $C_{bulk}^{-1} = C_{SC}^{-1} + C_H^{-1}$), with C_{SC} referring to the depletion layer inside the semiconductor and C_H

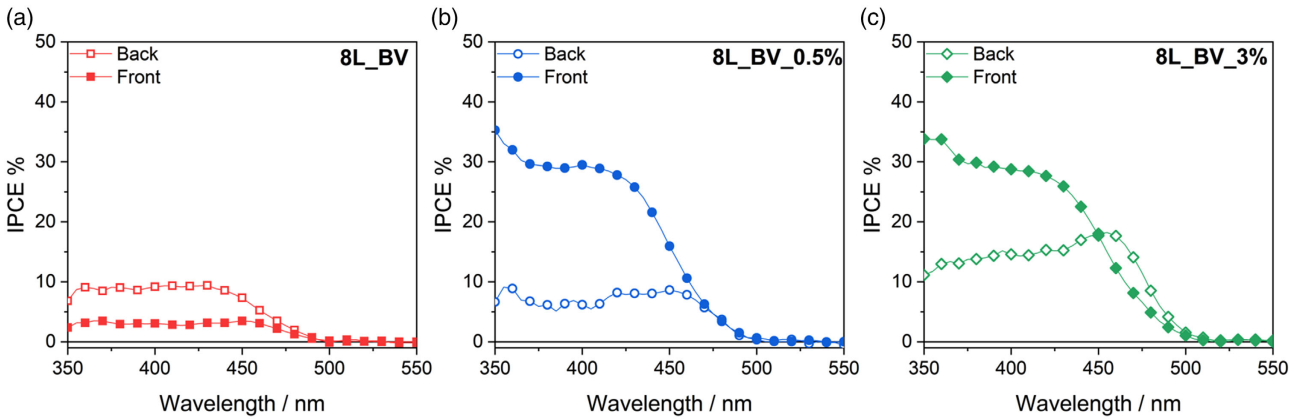

Figure 9. Incident photon to current efficiency (IPCE) plots of: a) 8L_BV, b) 8L_BV_0.5%, and c) 8L_BV_3% photoanodes under back- (void symbols) and front-side (full symbols) irradiation in a 0.5 M Na_2SO_4 electrolyte solution at 1.23 V versus RHE.

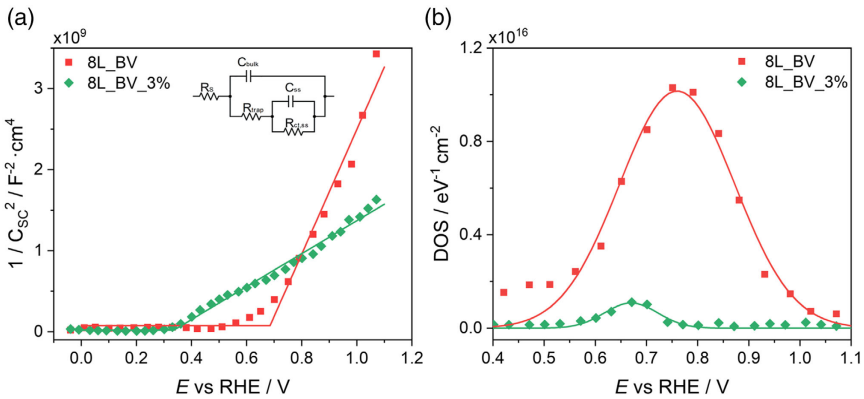

Figure 10. a) Mott–Schottky plots obtained with 8L_BV (red squares) and 8L_BV_3% (green diamonds) in 0.5 M Na_2SO_4 solution under irradiation, and relative fitting lines. b) Energy distribution of density of surface states (DOS) for 8L_BV (red squares) and 8L_BV_3% (green diamonds) fitted with a Gaussian function.

to the Helmholtz layer inside the electrolyte; iii) a parallel resistance of hole trapping to surface states R_{trap}; iv) a $C_{ss}/R_{ct,ss}$ pair corresponding to surface state capacitance C_{ss} and charge transfer resistance $R_{ct,ss}$ from surface states to oxidize water, respectively. The presence of the chemical surface state capacitance, associated with the accumulation/transfer of charges through potential surface states, makes this equivalent circuit (EC) an excellent approximation if charge transfer at the SCLJ is affected by the presence of surface states.[29,68]

From the Mott–Schottky (M–S) plots reported in Figure S12, Supporting Information, correlating the C_{SC} values extracted from impedance spectra recorded in the dark to the applied potential, the electron donor density N_D and flatband potential E_{FB} of the investigated electrodes were evaluated, according to the Randles model (inset of Figure S12, Supporting Information). The positive slopes of the well-defined linear region of both plots confirm the n-type character of pure and Mo^{6+}-doped BV materials. Extrapolation of the linear part of M–S plots provides E_{FB} values of 0.59 and 0.74 V versus. RHE for the pure BV_8L and doped 8L_BV_3% electrodes, respectively, as shown in Figure S12, Supporting Information, the former value being in good agreement with the E_{FB} reported for pure $BiVO_4$.[71] From the slope of the linear fits, N_D values of $4.79 \cdot 10^{19}$ and $1.97 \cdot 10^{20}$ cm^{-3} are obtained for pure 8L_BV and 8L_BV_3% electrodes, respectively, using a dielectric constant of 68[39] (**Table 4**). The linear portion of the C_{SC}^{-2} versus applied potential plot at higher potential was employed in the case of undoped BV. A fourfold enhancement in donor density is thus attained upon a 3 at% Mo^{6+} doping, consistent with the additional free electrons in the material bulk provided by the n-type dopant.[9,37,40,72]

Table 4. Flatband potential E_{FB} and donor density N_D obtained from EIS and total density of surface states N_{SS} under irradiation.

Electrode	E_{FB} vs. RHE [V]	N_D [cm]$^{-3}$	N_{SS} [cm]$^{-2}$
8L_BV	0.59	$4.79 \cdot 10^{19}$	$2.87 \cdot 10^{15}$
8L_BV_3%	0.74	$1.97 \cdot 10^{20}$	$1.41 \cdot 10^{14}$

The flat region in the M–S plot of pure BV recorded in the dark (Figure S12, Supporting Information), i.e., the lack of increase in C_{SC}^{-2} in the 0.6–0.9 V versus RHE region, may originate from Fermi-level pinning (FLP),[73–75] occurring when an increase of applied voltage results in the charging of surface states rather than in the increase of the semiconductor band bending.[76] In this case, most of the applied potential drop should occur across the Helmholtz layer rather than across the space charge region.[66,77] No FLP appears instead for the 8L_BV_3% electrode (Figure S12, Supporting Information).

The elaboration according to the EC model (inset of Figure 10a) of PEIS data collected with the two electrodes under irradiation allows extraction of the C_{SS} contribution, arising from charge accumulation at the SCLJ, which can be directly converted into the energy distribution density of surface states (DOS) under irradiation[29] by $C_{SS} = q \times DOS$, q being the elementary charge. The so calculated DOS for both 8L_BV and 8L_BV_3% electrodes are plotted in Figure 10b against the applied potential and fitted with a Gaussian function. A very intense and well-defined peak located at *ca.* 0.75 V versus RHE, which falls within the potential range of FLP in the dark (Figure S12, Supporting Information), characterizes the DOS curve relative to 8L_BV, while the 8L_BV_3% electrode exhibits only a much less pronounced peak at lower potential. A total density of surface states $N_{SS} = 2.87 \cdot 10^{15}$ cm^{-2} is obtained from the integration of the DOS versus potential curve of the 8L_BV film, while a much lower $N_{SS} = 1.41 \cdot 10^{14}$ cm^{-2} results from the integration of the DOS curve relative to the 8L_BV_3% electrode (Table 4).

The presence of charge accumulation in the undoped BV might be related to the shift of the relative M–S plot, recorded under irradiation, toward higher potential values compared to doped BV (Figure 10a), which should reflect a rigid downward shift of the band edges, caused by holes accumulation at the capacitive layer of pure 8L_BV.[78] Moreover, a high photovoltage is developed in the doped photoanode, as suggested by the large E_{FB} shift toward less positive potential evidenced in the doped electrode under irradiation compared to dark conditions (Figure S13b, Supporting Information), while no shift is observed in the case of the pure BV photoanode (Figure S13a, Supporting Information).

The suppression of this charge accumulation upon a 3 at% Mo^{6+} incorporation may be a consequence of Fermi-level unpinning in 8L_BV_3% with respect to 8L_BV. However, also a favorable hole extraction promoted by the observed gradient doping[79] in 8L_BV_3%, with a higher concentration of Mo^{6+} ions at the top of the film surface, or an accelerated oxygen evolution reaction by Mo segregation at the electrode surface, may not be discarded to be at the basis of the observed decrease in C_{SS} in doped BV with respect to pure BV.

Furthermore, Figure 10b shows that the DOS peak in doped BV appears at lower potential with respect to pure BV, in line with the relative trend in the M–S plots in Figure 10a, indicating that Mo^{6+} doping induces a change not only in the amount, but also in the energy level of surface states, so that an equal band bending extent would be obtained with a lower applied potential compared to pure BV.[77] This is also evidenced by the large gain in photovoltage observed for the doped electrode (Figure S13, Supporting Information),[80,81] as a consequence of the successful suppression of charge accumulation consequent to Mo^{6+} incorporation.

2.5. Mo Doping-Induced Surface Effects

PEIS analysis reveals that holes accumulate at the film/electrolyte interface in pure $BiVO_4$ in a concentration sufficiently high to act as surface states located at *ca.* 0.75 V versus RHE. Evidence of a surface state capacitance peak around 0.75 V versus RHE, associated with accumulated holes at the SCLJ,[73] was reported for pure or W^{6+}-doped BV and identified with the V^{5+}/V^{4+} redox process,[39,71,78] as well as the presence of IBG states in pure BV films, which are occupied by electrons in the dark and undergo depopulation upon application of an anodic bias, leading to accumulation of trapped holes at the material surface.[52,82] Surface V^{4+} states, due to oxygen vacancies formation, were also recently evidenced,[71] which can act as trapping sites of photoproduced holes located at an energetically unfavorable potential to drive water oxidation.

The surface state passivation upon Mo^{6+} dopant incorporation, in addition to the increased majority charge carrier concentration in the material bulk, results in the observed great enhancement in PEC performance in water oxidation attained with the 8L_BV_3% electrode with respect to pure $BiVO_4$. Thus, by taking into account present results together with recent literature reports, the mechanism shown in **Figure 11** is proposed to describe water oxidation at pure and Mo^{6+}-doped BV photoanodes.

The surface of pure BV in neutral conditions should be rich in V^{4+} states (occupied by electrons) formed after the localization of electrons from oxygen vacancies formation during the annealing process on neighboring V^{5+} sites. That is, the Fermi level in the dark E_F stays virtually fixed under increasing bias application until V^{4+} states are completely emptied, leaving unchanged the band bending degree and significantly lowering the photovoltage of the pure material. Upon irradiation, Fermi level splitting occurs into the quasi-Fermi levels of electrons ($E_{F,n}$) and holes ($E_{F,p}$), represented by the dashed lines in Figure 11, and such surface states can be progressively converted into photoproduced V^{5+} states, which are energetically unable to promote water oxidation, with the consequent detrimental accumulation of holes at the pure BV/water interface (Figure 11a).

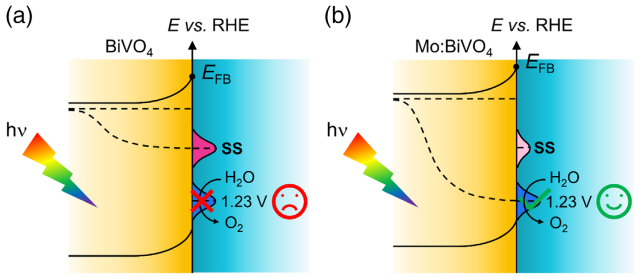

Figure 11. Mechanisms of PEC water oxidation on: a) pure and b) Mo^{6+}-doped $BiVO_4$. Solid lines indicate the valence band and conduction band of pure and Mo-doped BV, while dashed lines indicate the splitting of the Fermi level into electron and hole quasi-Fermi levels. The purple and blue density of states are representative of the surface states (SS) and of water oxidation intermediates, respectively.

When Mo^{6+} is introduced in BV, the additional free electrons supplied by the higher valent metal not only change the properties of the material bulk through the donor density N_D increase and consequent improvement in electron conductivity,[9,16–18,42,46] but also mitigates holes accumulation, as ascertained by the reduction of the capacitive peak C_{ss} in Figure 10b, with a huge decrease in N_{SS} with respect to pure BV. These findings result in an increased photovoltage for the doped material, so that $E_{F,p}$ can equilibrate with the water oxidation potential[70] at a lower potential than in pure BV,[83] leading to the conspicuous enhancement in water oxidation photocurrent (Figure 11b).

3. Conclusions

Mo^{6+} doping of $BiVO_4$ strongly impacts both bulk and surface properties of thin BV photoanodes. Besides the well-known role of the hexavalent n-type dopants in enhancing the electron conductivity of $BiVO_4$ by increasing the majority charge carrier density, and an elongation of the lifetime of photoproduced holes in the nano- to the microsecond time scale, here evidenced through TAS for the first time, a decrease in charge accumulation, induced by Mo doping, at the interface under irradiation is identified as a primary factor increasing the PEC performance of $BiVO_4$-based photoanodes. Multiple factors, including morphological, bulk and surface chemistry-induced effects, thus govern the photoactivity of Mo^{6+}-doped $BiVO_4$ photoanodes, which are at the basis of the outstanding improvement in their PEC performance upon doping.

4. Experimental Section

Chemicals and Materials: The following chemicals, purchased from Sigma Aldrich, were employed as supplied: bismuth(III) nitrate pentahydrate (≥98%), ammonium metavanadate (≥99%), molybdenum oxide bis(2,4-pentanedione) (≥99%), citric acid (99%), nitric acid 23.3%, sodium sulfate (≥99%), acetone. FTO glass, 2 mm thick, was purchased from Pilkington Glass (TEC-7).

Photoelectrodes Preparation: Pure BV electrodes were prepared according to a previously described procedure.[83] Typically, 0.002 mol of $Bi(NO_3)_3$ and NH_4VO_3 were added to 6 mL of 23.3% HNO_3 containing 0.004 mol of citric acid acting as a stabilizer. After complete dissolution of the precursors, a BV film layer was obtained by spinning 70 µL of the so obtained solution onto clean FTO at 8000 rpm for 30 s with an acceleration rate of 6000 rpm s^{-1}. The films were then dried at 80 °C for 10 min and annealed at 500 °C for 1 h in air. The thickness of the $BiVO_4$ layer was modulated by repeating the spin coating deposition and the thermal treatment up to 8 times. Prior to deposition, the FTO glass was cleaned by 30 min long sonication in a soap solution, followed by careful washing, sonication in ethanol for 30 min and drying in air. The clean glass was then cut into 2.5 × 2.5 cm^2 slices that underwent a 15 min-long UV-cleaner ozone treatment to remove any organic species deposited onto the FTO surface. Prior to deposition, the FTO slices were soaked in acetone for a few seconds to increase the quality of the resulting film. The Mo^{6+}-doped BV electrodes were synthesized by substituting the proper amount of Bi and V precursors with that of the molybdenum precursor in the starting solution, to obtain nominal molar dopant contents of 0.5 at% or 3.0 at% (i.e., mol (Mo)/[mol (Bi) + mol (V)] = 0.005 or 0.03, respectively). The so obtained precursor solutions were employed to prepare multilayer films of 0.5 at% or 3 at% Mo-doped BV with different thicknesses, by repeating the same spin coating procedure and annealing treatment adopted for pure BV up to 8 times. In all cases, films of both pure and doped BV with a high optical transparency were obtained regardless of the film thickness and the dopant content.

Characterization Methods: The crystalline phase of the materials was determined by collecting their XRD patterns using a Panalytical Empyrean system (Theta-Theta, 240 mm) equipped with a PIXcel-1D detector, Bragg–Brentano beam optics (including hybrid monochromator) and parallel beam optics. Raman spectra were measured with a LabRam spectrometer (Jobin Yvon Horiba) using a 532.19 nm excitation line provided by an Ar laser. SEM images were acquired using a Zeiss Gemini 300 scanning electron microscope in HV mode. Grain size was estimated employing the ImageJ software. UV−visible absorption spectra of the multilayer films were recorded in transmittance mode with a Jasco V-670 spectrophotometer. AFM images were measured using a Cypher S AFM from Asylum Research. XPS analyses were performed with PHI VersaProbe II scanning XPS microprobe (Physical Instruments AG, Germany) with a monochromatic Al Kα source with 24.8 W power with a beam size of 100 µm. Depth profile analysis was performed by etching the material with an argon ion sputter gun, at a rate (calibrated on SiO_2) of ~5.8 nm min^{-1} with a sampling depth of ~60 nm.

Transient Absoprtion Spectroscopy: Two electronically synchronized lasers were used in TAS measurements. An amplified femtosecond laser (Light Conversion Pharos) at 2 kHz repetition rate, with a central wavelength of 1024 nm and pulse duration of about 280 fs, was used for the generation of the probe pulses. The second harmonic at 512 nm was focused into a 3 mm sapphire plate to generate a broadband white light continuum spanning 380 to 490 nm. The third harmonic of a Q-switched Nd:YVO_4 laser (Innolas Picolo) with externally triggerable repetition rate, 355 nm central wavelength, and pulse duration of 500 ps, electronically triggered at 1 kHz and synchronized with respect to the femtosecond laser via an electronic delay, was used as a pump. It was focused on a 500 µm diameter spot at a fluence of 240 µJ cm^{-2}. The spectrum of the transmitted probe beam was measured by a high-speed spectrometer (Entwicklungsbuero EB Stresing) working at the full 2 kHz femtosecond laser repetition rate. Thanks to the electronic modulation of the pump pulse, two consecutive probe pulses measure the excited and unexcited sample, respectively.

Photoelectrochemical Characterization: PEC experiments were carried out using a three-electrode cappuccino-type electrochemical cell, where each of the BV-based photoanodes was setup as a working electrode with an active geometric area of 0.25 cm^2, a Pt wire as a counter electrode and a (Metrohm) Ag/AgCl (KCl sat'd) as the reference electrode. The cell was connected to a computer-controlled (EC-LAB V11.12) BioLogic SP-500 potentiostat to perform PEC measurements. Simulated AM 1.5 G solar irradiation was provided by a 1000 W Xe arc lamp (Newport Oriel), calibrated to the AM 1.5 G spectrum using a-Si photodiode sensor (S120VC, Thorlabs). During the tests, the BV-based photoanodes were illuminated from both the FTO substrate side (back irradiation) and the electrode/electrolyte side (front irradiation), with the electrode in contact with a 0.5 M Na_2SO_4 aqueous solution (pH 7). In all measurements, the applied potential, measured with respect to the Ag/AgCl reference electrode, was converted into the RHE scale based on the Nernst equation $E_{RHE} = E^{o}_{AgCl} + E_{AgCl} + 0.059 \times pH$. LSV measurements were performed at a scan rate of 20 mV s^{-1}. Ten consecutive LSV scans were recorded for all tested electrodes in each irradiation configuration, without ever observing any decay in photocurrent. IPCE measurements were collected using the same three-electrode configuration cappuccino-type cell, at a fixed applied potential of 1.23 V versus RHE. Monochromatic irradiation for IPCE tests was provided by a 75 W Xenon tunable PowerArc source (Optical Building Blocks) and the photon flux at each wavelength was measured with a S120VC (Thorlabs) photodiode power sensor. The IPCE curves were calculated as $IPCE = \frac{1240 \times J}{P_\lambda \times \lambda} \times 100$. The IQE plots were obtained by normalizing the corresponding IPCE curves for the photons absorbed by the material, obtained from the absorbance (A) spectrum, according to $IQE = \frac{IPCE(\lambda)}{1-10^{-A(\lambda)}}$. EIS measurements were carried out using a Bio-Logic SP-500 potentiostat coupled with the EC-Lab (V11.12) electrochemical platform, either in the dark or under AM 1.5 G simulated solar light provided by a 1000 W Xe arc lamp (Newport Oriel). During each PEIS scan, a voltage perturbation within a frequency range from 1to 50 mHz was applied with a 25 mV sinusoidal amplitude. A custom program written in the Python programming language was used to process and fit PEIS data.

Supporting Information

Supporting Information is available from the Wiley Online Library or from the author.

Acknowledgements

This work received partial financial support from the MIUR PRIN 20173397R7 MULTI-e project.

Open Access Funding provided by Universita degli Studi di Milano within the CRUI-CARE Agreement.

Conflict of Interest

The authors declare no conflict of interest.

Data Availability Statement

The data that support the findings of this study are available from the corresponding author upon reasonable request.

Keywords

bismuth vanadate, bulk charge transport, impedance spectroscopy, molybdenum doping, photoelectrochemistry, surface states passivation, water oxidation

Received: May 4, 2022
Published online:

[1] M. Grätzel, *Nature* **2001**, *414*, 338.
[2] N. S. Lewis, D. G. Nocera, *Proc. Natl. Acad. Sci.* **2006**, *103*, 15729.
[3] N. S. Lewis, *Science* **2016**, *351*, aad1920.

[4] M. G. Walter, E. L. Warren, J. R. McKone, S. W. Boettcher, Q. Mi, E. A. Santori, N. S. Lewis, *Chem. Rev.* **2010**, *110*, 6446.
[5] M. S. Prévot, K. Sivula, *J. Phys. Chem. C* **2013**, *117*, 17879.
[6] C. R. Lhermitte, A. Polo, L. Yao, F. A. Boudoire, N. Guijarro, K. Sivula, *ChemSusChem* **2020**, *13*, 3645.
[7] D. K. Lee, D. Lee, M. A. Lumley, K.-S. Choi, *Chem. Soc. Rev.* **2019**, *48*, 2126.
[8] Y. Kuang, Q. Jia, G. Ma, T. Hisatomi, T. Minegishi, H. Nishiyama, M. Nakabayashi, N. Shibata, T. Yamada, A. Kudo, K. Domen, *Nat. Energy* **2017**, *2*, 16191.
[9] Y. Park, K. J. McDonald, K.-S. Choi, *Chem. Soc. Rev.* **2013**, *42*, 2321.
[10] J. H. Kim, J. S. Lee, *Adv. Mater.* **2019**, *31*, 1.
[11] F. F. Abdi, R. van de Krol, *J. Phys. Chem. C* **2012**, *116*, 9398.
[12] K. Sivula, R. van de Krol, *Nat. Rev. Mater.* **2016**, *1*, 15010.
[13] C. Zachäus, F. F. Abdi, L. M. Peter, R. Van De Krol, *Chem. Sci.* **2017**, *8*, 3712.
[14] Y. Yang, S. Niu, D. Han, T. Liu, G. Wang, Y. Li, *Adv. Energy Mater.* **2017**, *7*, 1700555.
[15] J. Brillet, J.-H. Yum, M. Cornuz, T. Hisatomi, R. Solarska, J. Augustynski, M. Graetzel, K. Sivula, *Nat. Photonics* **2012**, *6*, 824.
[16] K. P. S. Parmar, H. J. Kang, A. Bist, P. Dua, J. S. Jang, J. S. Lee, *ChemSusChem* **2012**, *5*, 1926.
[17] W. Luo, Z. Yang, Z. Li, J. Zhang, J. Liu, Z. Zhao, Z. Wang, S. Yan, T. Yu, Z. Zou, *Energy Environ. Sci.* **2011**, *4*, 4046.
[18] W. J. Yin, S. H. Wei, M. M. Al-Jassim, J. Turner, Y. Yan, *Phys. Rev. B: Condens. Matter Mater. Phys.* **2011**, *83*, 1.
[19] A. J. E. Rettie, H. C. Lee, L. G. Marshall, J. Lin, C. Capan, J. Lindemuth, J. S. McCloy, J. Zhou, A. J. Bard, C. B. Mullins, *J. Am. Chem. Soc.* **2013**, *135*, 11389.
[20] H. S. Park, K. E. Kweon, H. Ye, E. Paek, G. S. Hwang, A. J. Bard, *J. Phys. Chem. C* **2011**, *115*, 17870.
[21] W. Luo, J. Wang, X. Zhao, Z. Zhao, Z. Li, Z. Zou, *Phys. Chem. Chem. Phys.* **2013**, *15*, 1006.
[22] B. Pattengale, J. Huang, *Phys. Chem. Chem. Phys.* **2016**, *18*, 32820.
[23] L. Yang, Y. Xiong, W. Guo, J. Guo, D. Gao, Y. Zhang, P. Xiao, *Electrochim. Acta* **2017**, *256*, 268.
[24] L. Chen, F. M. Toma, J. K. Cooper, A. Lyon, Y. Lin, I. D. Sharp, J. W. Ager, *ChemSusChem* **2015**, *8*, 1066.
[25] V. Nair, C. L. Perkins, Q. Lin, M. Law, *Energy Environ. Sci.* **2016**, *9*, 1412.
[26] M. Huang, J. Bian, W. Xiong, C. Huang, R. Zhang, *J. Mater. Chem. A* **2018**, *6*, 3602.
[27] L. Gao, X. Long, S. Wei, C. Wang, T. Wang, F. Li, Y. Hu, J. Ma, J. Jin, *Chem. Eng. J.* **2019**, *378*, 122193.
[28] W. Zhang, F. Wu, J. Li, D. Yan, J. Tao, Y. Ping, M. Liu, *ACS Energy Lett.* **2018**, *3*, 2232.
[29] B. Klahr, S. Gimenez, F. Fabregat-Santiago, T. Hamann, J. Bisquert, *J. Am. Chem. Soc.* **2012**, *134*, 4294.
[30] A. Polo, I. Grigioni, M. Magni, A. Facibeni, M. V. Dozzi, E. Selli, *Appl. Surf. Sci.* **2021**, *556*, 149759.
[31] H. Ye, J. Lee, J. S. Jang, A. J. Bard, *J. Phys. Chem. C* **2010**, *114*, 13322.
[32] S. S. Mali, G. R. Park, H. Kim, H. H. Kim, J. V. Patil, C. K. Hong, *Nanoscale Adv.* **2019**, *1*, 799.
[33] M. Tayebi, A. Tayyebi, B. K. Lee, *Sol. Energy* **2019**, *191*, 427.
[34] H. Jung, S. Y. Chae, H. Kim, B. K. Min, Y. J. Hwang, *Catal. Commun.* **2016**, *75*, 18.
[35] M. Tayebi, A. Tayyebi, B. K. Lee, *Catal. Today* **2019**, *328*, 35.
[36] M. W. Kim, K. Kim, T. Y. Ohm, B. Joshi, E. Samuel, M. T. Swihart, H. Yoon, H. Park, S. S. Yoon, *J. Alloys Compd.* **2017**, *726*, 1138.
[37] Y. Park, D. Kang, K.-S. Choi, *Phys. Chem. Chem. Phys.* **2014**, *16*, 1238.
[38] J. R. C. Junqueira, T. Bobrowski, O. A. Krysiak, R. Gutkowski, W. Schuhmann, *ChemCatChem* **2019**, *11*, 6417.
[39] Q. Shi, S. Murcia-López, P. Tang, C. Flox, J. R. Morante, Z. Bian, H. Wang, T. Andreu, *ACS Catal.* **2018**, *8*, 3331.
[40] H. W. Jeong, T. H. Jeon, J. S. Jang, W. Choi, H. Park, *J. Phys. Chem. C* **2013**, *117*, 9104.
[41] M. Rohloff, B. Anke, S. Zhang, U. Gernert, C. Scheu, M. Lerch, A. Fischer, *Sustain. Energy Fuels* **2017**, *1*, 1830.
[42] F. F. Abdi, T. J. Savenije, M. M. May, B. Dam, R. van de Krol, *J. Phys. Chem. Lett.* **2013**, *4*, 2752.
[43] W. Q. Hong, *J. Phys. D. Appl. Phys.* **1989**, *22*, 1384.
[44] S. Murcia-López, C. Fàbrega, D. Monllor-Satoca, M. D. Hernández-Alonso, G. Penelas-Pérez, A. Morata, J. R. Morante, T. Andreu, *ACS Appl. Mater. Interfaces* **2016**, *8*, 4076.
[45] R. P. Antony, M. Zhang, K. Zhou, S. C. J. Loo, J. Barber, L. H. Wong, *ACS Omega* **2018**, *3*, 2724.
[46] S. K. Pilli, T. E. Furtak, L. D. Brown, T. G. Deutsch, J. A. Turner, A. M. Herring, *Energy Environ. Sci.* **2011**, *4*, 5028.
[47] R. P. Antony, P. S. Bassi, F. F. Abdi, S. Y. Chiam, Y. Ren, J. Barber, J. S. C. Loo, L. H. Wong, *Electrochim. Acta* **2016**, *211*, 173.
[48] T. H. Jeon, H. Kim, H. Kim, W. Choi, *Energy Environ. Sci.* **2020**, *13*, 1730.
[49] T. Li, J. He, B. Peña, C. P. Berlinguette, *Angew. Chemie - Int. Ed.* **2016**, *55*, 1769.
[50] W. Yao, H. Iwai, J. Ye, *Dalt. Trans.* **2008**, 1426.
[51] W. Luo, Z. Li, T. Yu, Z. Zou, *J. Phys. Chem. C* **2012**, *116*, 5076.
[52] J. Ravensbergen, F. F. Abdi, J. H. Van Santen, R. N. Frese, B. Dam, R. Van De Krol, J. T. M. Kennis, *J. Phys. Chem. C* **2014**, *118*, 27793.
[53] B. Pattengale, J. Huang, *Phys. Chem. Chem. Phys.* **2017**, *19*, 6831.
[54] B. Pattengale, J. Ludwig, J. Huang, *J. Phys. Chem. C* **2016**, *120*, 1421.
[55] I. Grigioni, K. G. Stamplecoskie, E. Selli, P. V. Kamat, *J. Phys. Chem. C* **2015**, *119*, 20792.
[56] I. Grigioni, M. Abdellah, A. Corti, M. V. Dozzi, L. Hammarström, E. Selli, *J. Am. Chem. Soc.* **2018**, *140*, 14042.
[57] A. Polo, F. , C. R. Lhermitte, Y. Liu, N. Guijarro, M. V. Dozzi, E. Selli, K. Sivula, *J. Mater. Chem. A* **2021**, *9*, 27736.
[58] S. Selim, L. Francàs, M. García-Tecedor, S. Corby, C. Blackman, S. Gimenez, J. R. Durrant, A. Kafizas, *Chem. Sci.* **2019**, *10*, 2643.
[59] L. Steier, I. Herraiz-Cardona, S. Gimenez, F. Fabregat-Santiago, J. Bisquert, S. D. Tilley, M. Grätzel, *Adv. Funct. Mater.* **2014**, *24*, 7681.
[60] O. Zandi, B. M. Klahr, T. W. Hamann, *Energy Environ. Sci.* **2013**, *6*, 634.
[61] Y. Liang, T. Tsubota, L. P. A. Mooij, R. van de Krol, *J. Phys. Chem. C* **2011**, *115*, 17594.
[62] F. Le Formal, M. Grätzel, K. Sivula, *Adv. Funct. Mater.* **2010**, *20*, 1099.
[63] C. Liu, H. Luo, Y. Xu, Z. Zhang, Q. Liang, W. Wang, Z. Chen, *Chem. Eng. J.* **2020**, *384*, 123333.
[64] J. Brillet, M. Comuz, F. Le Formal, J. H. Yum, M. Grätzel, K. Sivula, *J. Mater. Res.* **2010**, *25*, 17.
[65] M. S. Prévot, Y. Li, N. Guijarro, K. Sivula, *J. Mater. Chem. A* **2016**, *4*, 3018.
[66] Y. Liu, F. Le Formal, F. , L. Yao, K. Sivula, N. Guijarro, *J. Mater. Chem. A* **2019**, *7*, 1669.
[67] M. S. Prévot, X. A. Jeanbourquin, W. S. Bourée, F. Abdi, D. Friedrich, R. Van De Krol, N. Guijarro, F. Le Formal, K. Sivula, *Chem. Mater.* **2017**, *29*, 4952.
[68] L. Bertoluzzi, P. Lopez-Varo, J. A. Jiménez Tejada, J. Bisquert, *J. Mater. Chem. A* **2016**, *4*, 2873.
[69] G. V. Govindaraju, G. P. Wheeler, D. Lee, K.-S. Choi, *Chem. Mater.* **2017**, *29*, 355.
[70] X. Zhao, J. Hu, B. Wu, A. Banerjee, S. Chakraborty, J. Feng, Z. Zhao, S. Chen, R. Ahuja, T. C. Sum, Z. Chen, *J. Mater. Chem. A* **2018**, *6*, 16965.

[71] S. Selim, E. Pastor, M. García-Tecedor, M. R. Morris, L. Francàs, M. Sachs, B. Moss, S. Corby, C. A. Mesa, S. Gimenez, A. Kafizas, A. A. Bakulin, J. R. Durrant, *J. Am. Chem. Soc.* **2019**, *141*, 18791.
[72] Y. S. Chen, L. Y. Lin, J. S. Ma, *Electrochim. Acta* **2020**, *329*, 135171.
[73] A. J. Bard, A. B. Bocarsly, F. R. F. Fan, E. G. Walton, M. S. Wrighton, *J. Am. Chem. Soc.* **1980**, *102*, 3671.
[74] H. J. Lewerenz, *J. Electroanal. Chem.* **1993**, *356*, 121.
[75] A. J. B. G. Nagasubramanian, B. L. Wheeler, *J. Electrochem. Soc.* **1983**, *130*, 1680.
[76] N. Sato, *Electrochemistry at Metal and Semiconductor Electrodes*, first ed., Elsevier, Amsterdam **1998**.
[77] K. Sivula, *J. Phys. Chem. Lett.* **2013**, *4*, 1624.
[78] B. J. Trześniewski, I. A. Digdaya, T. Nagaki, S. Ravishankar, I. Herraiz-Cardona, D. A. Vermaas, A. Longo, S. Gimenez, W. A. Smith, *Energy Environ. Sci.* **2017**, *10*, 1517.
[79] F. F. Abdi, L. Han, A. H. M. Smets, M. Zeman, B. Dam, R. van de Krol, *Nat. Commun.* **2013**, *4*, 2195.
[80] O. Zandi, T. W. Hamann, *J. Phys. Chem. Lett.* **2014**, *5*, 1522.
[81] B. J. Trześniewski, W. A. Smith, *J. Mater. Chem. A* **2016**, *4*, 2919.
[82] I. Grigioni, L. Ganzer, F. V. A. Camargo, B. Bozzini, G. Cerullo, E. Selli, *ACS Energy Lett.* **2019**, *4*, 2213.
[83] I. Grigioni, K. G. Stamplecoskie, D. H. Jara, M. V. Dozzi, A. Oriana, G. Cerullo, P. V. Kamat, E. Selli, *ACS Energy Lett.* **2017**, *2*, 1362.